

Designing quantum technologies with a quantum computer

Juan Naranjo¹ , Thi Ha Kyaw¹ ,* Gaurav Saxena¹ , Kevin Ferreira¹, and Jack S. Baker¹ †

¹*LG Electronics Toronto AI Lab*

(Dated: January 30, 2026)

Interacting spin systems in solids underpin a wide range of quantum technologies, from quantum sensors and single-photon sources to spin-defect-based quantum registers and processors. We develop a quantum-computer-aided framework for simulating such devices using a general electron spin resonance Hamiltonian incorporating zero-field splitting, the Zeeman effect, hyperfine interactions, dipole-dipole spin-spin terms, and electron-phonon decoherence. Within this model, we combine Gray-encoded qudit-to-qubit mappings, qubit-wise commuting aggregation, and a multi-reference selected quantum Krylov fast-forwarding (sQKFF) hybrid algorithm to access long-time dynamics while remaining compatible with NISQ and early fault-tolerant hardware constraints. Numerical simulations demonstrate the computation of autocorrelation functions up to ~ 100 ns, together with microwave absorption spectra and the ℓ_1 -norm of coherence, achieving 18-30% reductions in gate counts and circuit depth for Trotterized time-evolution circuits compared to unoptimized implementations. Using the nitrogen vacancy center in diamond as a testbed, we benchmark the framework against classical simulations and identify the reference-state selection in sQKFF as the primary factor governing accuracy at fixed hardware cost. This methodology provides a flexible blueprint for using quantum computers to design, compare, and optimize solid-state spin-qubit technologies under experimentally realistic conditions.

I. INTRODUCTION

Solid state materials embedded with spin-active defects are increasingly attracting attention for their potential applications as quantum sensors, single-photon sources, quantum processors and more. The search for new spin defects and suitable host materials is an active area of research, where candidate systems must allow for precise manipulation and readout and permit long coherence times [1–4]. Among these systems, nitrogen-vacancy (NV) centers have emerged as a leading platform due to their long coherence, dephasing, and relaxation times, which can be further extended through techniques such as Ramsey and Hahn echo sequences [5, 6]. Nevertheless, the complex spin-environment interactions and internal spin couplings pose significant challenges for classical modeling and analysis [7, 8]. Digital quantum computer-aided design [9, 10] offers a promising alternative, enabling the investigation of essential properties, such as the coherence times of arbitrary states, the study of system dynamics under realistic experimental conditions, and the numerous useful properties which may be computed using these dynamics, including absorption spectra and more.

More broadly, the simulation of quantum systems [11] stands as one of the most promising applications of quantum computing, alongside drug discovery [12, 13], communications [14, 15], optimization [16, 17], machine learning [18–20], and cryptography [21, 22]. Nevertheless, current quantum technologies still operate within the Noisy Intermediate-Scale Quantum (NISQ) era, transitioning toward early fault-tolerant devices, where lim-

ited resources and intrinsic noise constrain hardware [23, 24]. Therefore, a central research direction is the development of efficient algorithms that can approximate the time evolution of quantum systems while minimizing the required computational resources. Key optimization metrics include the number of single- and multi-qubit gates, qubit counts, and circuit depth, thereby mitigating restrictions imposed by various sources of noise [25, 26].

Spin Hamiltonians serve as coarse-grained models in chemistry and materials science, capturing collective magnetic interactions in a simplified form. When calibrated with accurate parameters, such effective models can reproduce complex phenomena, yet they remain many-body in nature and are generally intractable for classical computation. A prominent example is the nuclear magnetic resonance (NMR) spin Hamiltonian, which has become a focus of recent quantum simulation efforts on gate-based processors. A recent demonstration of quantum advantage, for instance, demonstrated that simulation of higher-order out-of-time-ordered correlators (OTOCs) is likely beyond the reach of classical supercomputers [27]. They later showed that OTOC data harvested from NMR experiments in what they call many-body nuclear spin echo sequences may be used to train parameterized OTOC in an NMR Hamiltonian learning setup to extract molecular geometric information [28, 29]. While NMR-type models have provided a valuable testbed for quantum simulation, the electron spin resonance (ESR) Hamiltonian, which we explore in this work, extends this paradigm by incorporating both electronic and nuclear spins along with spin-phonon interactions.

Together, our approach describes a collection of interacting spin defects distributed inside a real solid with vibrational degrees of freedom. This class of ESR spin-defect models, which underpins platforms like the NV

* thiha.kyaw@lge.com

† jack.baker@lge.com

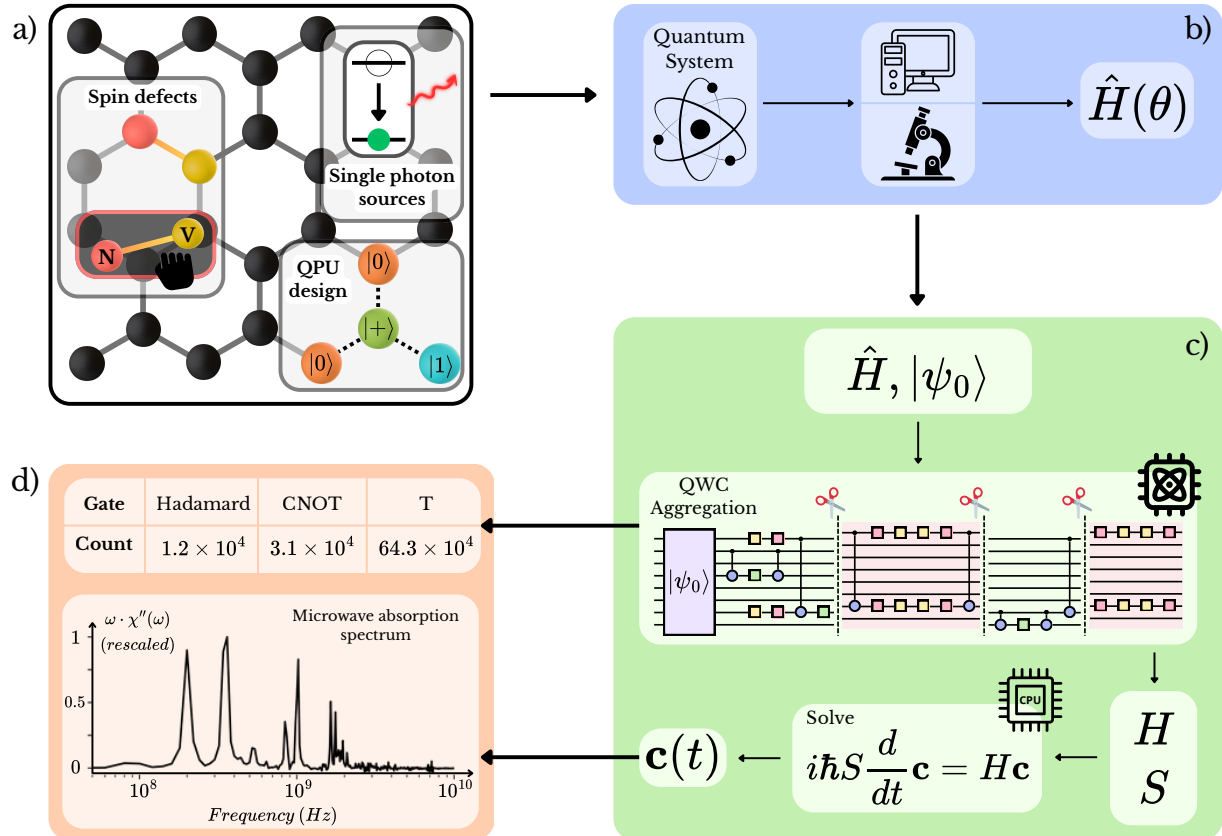


FIG. 1. The quantum computer-aided design framework proposed in this work. The process begins by defining a quantum system (a) by specifying spin-defect species, the host material, the presence of nuclear spin species, applied magnetic fields, and the geometry of the spin ensemble (configurations 1, 2, and 3 in Table I are examples of such a specification). Next, the system Hamiltonian is constructed, with its parameters obtained either computationally or experimentally, as depicted in (b). With the Hamiltonian defined, the sQKFF algorithm can be executed by specifying the system's initial state. (c) is divided into two parts: the quantum component, which computes the elements of the H and S matrices via Hadamard tests and performs the optimization step through QWC aggregation; and the classical component, which solves the Schrödinger equation within the Krylov subspace. Finally, as shown in (d), the outputs of (c) enable the estimation of quantum resource requirements and the computation of key system properties such as the system's autocorrelation function, microwave absorption spectrum, and time-dependent ℓ_1 -norm of coherence of other dynamics-derived properties.

center, has received comparatively little attention in the quantum simulation literature despite its application to realistic quantum technologies. Only very recently have studies begun exploring quantum algorithms for simulating spin defects in solids [30–32], often by tackling the full electronic structure problem (or a reduced electronic structure problem by utilizing embedding theories [33, 34]) at great computational cost. By contrast, focusing on an ESR Hamiltonian with an effective spin–boson coupling, as we do in this work, is far more economical in quantum resources than treating electron–phonon interactions from first principles, yet can retain the essential physics needed to design and optimize spin-based quantum technologies.

In this work, we present a framework for simulating and characterizing spin defects in solid-state materials, enabling deeper analysis of current experimental

platforms and exploration of new candidates for next-generation quantum technologies. As illustrated in Fig. 1, the methodology integrates techniques optimized for computational efficiency on existing quantum hardware and is validated across three distinct NV[−] center configurations. The procedure begins by defining a spin defect system in a particular material, whose Hamiltonian parameters are either taken from experimental data or computed using classical methods on a high performance computer. We then encode the system's Hamiltonian into a spin-1/2 representation for time-evolution simulation and computation of relevant properties. However, operational quantities such as coherence and dephasing times manifest over long timescales, from nanoseconds to microseconds [5], making conventional approaches such as the Trotter–Suzuki decomposition computationally unfeasible [35]. Hybrid algorithms have

Configuration	1	2	3
Specific parameters	- 1 NV ⁻ centre - $ \varphi\rangle = \frac{1}{\sqrt{2}}(0\rangle + 2\rangle)$	- 3 NV ⁻ centres - $ \varphi\rangle = \frac{1}{\sqrt{2}}(000\rangle + 222\rangle)$	- 1 NV ⁻ centre - 2 N ¹⁴ impurities - $ \varphi\rangle = \frac{1}{\sqrt{2}}(0\rangle + 2\rangle)$
Common parameters	- Magnetic field of 2 mT in the z direction - Boson bath of dimension 8, with a single frequency mode of 5.8 GHz - Spin-boson coupling intensity of 1.78 GHz and coupling operator S_x - Initial state of the bath: $Ry\left(\frac{\pi}{2}\right) \otimes Ry\left(\frac{\pi}{4}\right) \otimes Ry\left(\frac{\pi}{8}\right) 000\rangle$ - Initial state of each NV ⁻ nuclear spin and/or N ¹⁴ impurity: $ 0\rangle$		

TABLE I. Parameters of the three NV⁻ centre configurations and their interactions. $|\varphi\rangle$ denotes the initial state of the electronic spin of the NV⁻ centres, with $|2\rangle \equiv |m_s = +1\rangle$. In configurations 2 and 3, the three components, NV⁻s and/or N¹⁴ impurities, are arranged at the vertices of an equilateral triangle with a side length of 1 nm.

emerged to address this limitation by fast-forwarding time evolution with fewer resources [36–40]. Among them, the *multi-reference, selected Quantum Krylov Fast-Forwarding* (sQKFF) algorithm [41] offers a practical approach by extending its dependence from the simulated time to the number of reference states used to approximate long-time dynamics, while significantly reducing key metrics such as gate count and circuit depth. Our framework further integrates an optimization stage based on qubit-wise commuting (QWC) aggregation [42, 43], which improves the reduction of resource requirements.

The remainder of this work is organized as follows. Section II provides a detailed explanation of each step of the proposed framework, including key methodological considerations and descriptions of the NV⁻ configurations used in numerical simulation. Section III presents the results, focusing on the comparison between properties approximated using both the sQKFF algorithm and QuTiP, including an analysis of the influence of varying the Trotterization error and the number of reference states, R , in the sQKFF algorithm. Resource estimations are presented in this section. Section IV discusses additional factors that may affect the results and outlines potential directions for future research. Finally, Section V summarizes the main findings and conclusions of this work.

II. METHODS

A. Hamiltonian Models for Spin-Defects Simulations.

To ensure simulations closely resemble experimental conditions, and thus support the prototyping of spin de-

fects in solid-state materials, the framework incorporates a range of relevant interactions: from operational ones, such as the coupling to external magnetic fields, to environmental effects including lattice vibrations and nearby spin impurities. In addition, recent lines of investigation are moving towards designing Hamiltonians of materials with desired properties [44], which, if expressed in terms of Pauli strings, can also be simulated with the present framework. A detailed discussion of the Hamiltonian terms used in this work can be found in [5, 7, 45].

In the remainder of this section, we present the Hamiltonian for a system of interacting NV⁻ spin defects. The same form applies to other spin-defect platforms and host materials, with the appropriate choice of Hamiltonian parameters. To describe the dynamics of a system with \mathcal{N} NV⁻ centers, the zero-field splitting and Zeeman terms,

$$\hat{H}_S = \hbar D \sum_{i=1}^{\mathcal{N}} \hat{S}_{z,i}^2 + g_{NV} \mu_B \vec{B} \cdot \sum_{i=1}^{\mathcal{N}} \vec{S}_i, \quad (1)$$

are included. These describe the electronic spins' interaction with an external magnetic field \vec{B} . Here, $D = 2.87$ GHz denotes the zero-field splitting parameter, $g_{NV} = 2.003$ the NV g-factor, μ_B the Bohr magneton, and $\vec{S}_i = [S_{x,i}, S_{y,i}, S_{z,i}]$ the electronic spin-1 operator of the i -th NV⁻ center [5, 46].

The hyperfine interaction between the electronic spin and the ¹⁴N nuclear spin of the NV⁻ centers is described by

$$\hat{H}_N = g_N \mu_N \vec{B} \cdot \sum_{i=1}^{\mathcal{N}} \vec{I}_i + \hbar \sum_{i=1}^{\mathcal{N}} \left[A_{\parallel} \hat{S}_{z,i} \hat{I}_{z,i} + A_{\perp} \left(\hat{S}_{x,i} \hat{I}_{x,i} + \hat{S}_{y,i} \hat{I}_{y,i} \right) + Q \left(\hat{I}_{z,i}^2 - \frac{2}{3} \hat{I}_i \right) \right], \quad (2)$$

with $g_N = 0.403573$ the nuclear g-factor, μ_N the nuclear magneton, $A_{\parallel} = -2.16$ MHz and $A_{\perp} = -2.7$ MHz

the axial and transverse hyperfine coupling constants,

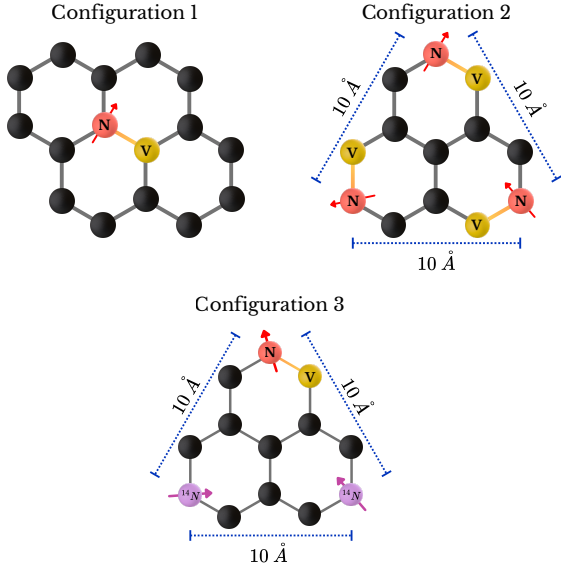


FIG. 2. Layout of the three configurations of NV^- centers, represented as yellow and red elements, and ^{14}N impurities, represented as purple elements.

$Q = 5$ MHz the nuclear electric quadrupole parameter, and $\vec{I}_i = [I_{x,i}, I_{y,i}, I_{z,i}]$ the spin-1 operator of the i -th NV^- center's ^{14}N nucleus [5, 46, 47]. Note that the Zeeman and quadrupole terms in Eq. 2 correspond to the dynamics of a ^{14}N impurity within the lattice.

Since one of the primary sources of decoherence in spin defects arises from coupling to lattice vibrations, an interaction modeled through the spin–boson Hamiltonian

$$\hat{H}_B = \hbar\omega\hat{b}^\dagger\hat{b} + \hbar\lambda \sum_{i=1}^N \hat{S}_{x,i} \otimes (\hat{b}^\dagger + \hat{b}), \quad (3)$$

where ω is the phonon mode frequency, λ the coupling strength, and b , b^\dagger the annihilation and creation operators. Notice that Eq. 3 corresponds to a boson bath with a single vibration mode coupled to all NV^- centers. This Hamiltonian can be extended to include boson baths with multiple vibration modes that can be coupled to various spin elements within the considered layout. An additional source of decoherence is nearby spins, such as other NV^- centers' electronic spins or ^{14}N impurities' spins. This interaction is captured via the dipole–dipole Hamiltonian, described by

$$\hat{H}_{dd} = \frac{\mu_0\alpha_1\alpha_2}{4\pi r^3} [\vec{S}_1 \cdot \vec{S}_2 - 3(\vec{S}_1 \cdot \hat{r})(\vec{S}_2 \cdot \hat{r})], \quad (4)$$

with μ_0 the vacuum permeability; then, for each spin 1 and 2: α the product of their respective g-factor and magneton, and \vec{S} is their spin operator. These spins are separated by an r distance, with \hat{r} the unitary direction vector.

Evidently, a wide range of possible configurations exists within each platform, even within the specific case of

NV^- centers, and our framework is designed to be applicable across all such scenarios. As a testbed for analyzing the influence of each interaction and enabling cross-comparison, three distinct NV^- configurations were simulated using the proposed framework, with their parameters summarized in Tab. I and their layouts sketched in Fig. 2. To enable efficient simulation, the d -level Hamiltonians are mapped into a spin-1/2 representation using Gray encoding, yielding a qubit count that scales as $\lceil \log_2(d) \rceil$ [48].

B. Qubit-wise Commuting Partitioning and Circuit Optimization

The resulting Hamiltonian, \hat{H} , expressed as a sum of Pauli strings, is partitioned into qubit-wise commuting (QWC) groups. In each group, all terms commute within corresponding qubit subspaces, allowing a set of single-qubit Clifford rotations to simultaneously diagonalize the group [42, 43]. This property is particularly useful when implementing time evolution via Trotterization, as it enables the use of canonical circuits for exponentiating the diagonal Pauli strings [48]. The grouping further allows optimal reordering of exponentials, so that adjacent adjoint operations cancel, effectively reducing both the number of gates and the overall circuit depth.

C. The sQKFF algorithm

Once an efficient way to approximate the time evolution operator is determined, the sQKFF algorithm can be applied. It yields an approximation of the time-evolved state given by

$$|\psi(t)\rangle = e^{-it\hat{H}/\hbar} |\psi_0\rangle \approx \sum_{m=0}^{M-1} \sum_{r=1}^R c_{mr}(t) |\phi_{mr}\rangle, \quad (5)$$

with $|\psi_0\rangle$ the initial state, c_{mr} a time-dependent complex coefficient, and $|\phi_{mr}\rangle$ a reference state. This approximation constructs the M -order Krylov subspace with a number R of reference states. These reference states have the form $|\phi_{mr}\rangle = e^{-im\tau\hat{H}} |r\rangle$, where $|r\rangle \in \{|\psi_0\rangle, |\mathcal{B}_1\rangle, \dots, |\mathcal{B}_{R-1}\rangle\}$, and each \mathcal{B}_r denotes a bitstring reference state, obtained by measuring the state $e^{-i(M-1)\tau\hat{H}} |\psi_0\rangle$ and selected according to its measurement probability. Replacing Eq. 5 into Schrödinger's equation and multiplying both sides by $\langle \phi_{m'r'} |$ yields

$$i\hbar S \frac{\partial}{\partial t} \mathbf{c} = H \mathbf{c}, \quad (6)$$

where S and H are $MR \times MR$ matrices with elements $\langle \phi_{m'r'} | \phi_{mr} \rangle$ and $\langle \phi_{m'r'} | \hat{H} | \phi_{mr} \rangle$, respectively, and \mathbf{c} is a $MR \times 1$ coefficient vector. Since the reference states $|\phi_{mr}\rangle$ are defined using the *exact* time-evolution operator, which commutes with \hat{H} and satisfies $e^{it'\hat{H}} e^{-it\hat{H}} =$

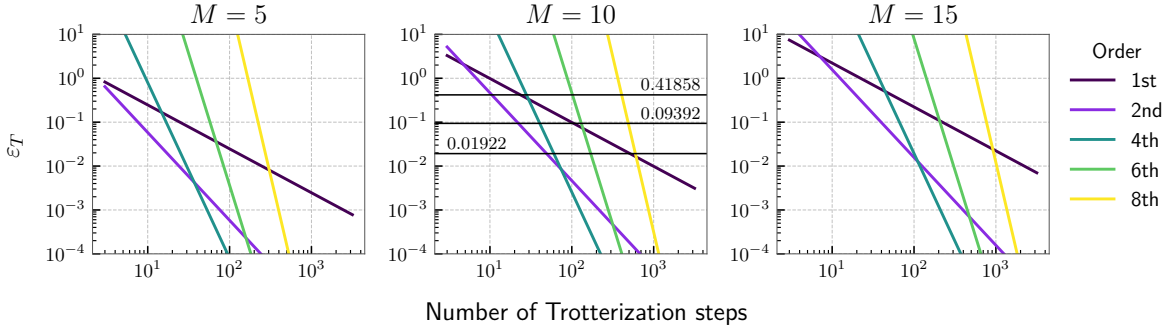


FIG. 3. Trotterization error ε_T , bounded with the Hamiltonian's 1-norm $\|\hat{H}\|_1$, as a function of the number of Trotter steps, shown for different values of M : the Krylov subspace order.

$e^{-i(t-t')\hat{H}}$, a Toeplitz structure for S and H can be considered, which reduces the total number of matrix elements to be estimated to $\approx MR + \frac{1}{2}(2M - 1)(R - 1)R$. The form of these elements is

$$\begin{aligned} S_{m'm', mr} &= \left\langle r' \left| e^{-i(m-m')\tau\hat{H}} \right| r \right\rangle \\ H_{m'm', mr} &= \left\langle r' \left| \hat{H} e^{-i(m-m')\tau\hat{H}} \right| r \right\rangle. \end{aligned} \quad (7)$$

Solving Eq. 6 is the classical component of the algorithm, while the quantum component consists of evaluating the matrix elements of S and H from Eq. 7, which in this work were computed using Hadamard tests with second-order Trotterizations to approximate the time-evolution operator.

Cortés and Gray [49] provide a bound for the sQKFF parameter τ based on the spectral range of the Hamiltonian, ΔE , namely $\tau \leq \frac{\pi\hbar}{\Delta E}$. Using this result and the fact that $\|\hat{H}\|_1 \geq \Delta E/2$, where $\|\hat{H}\|_1$ denotes the Hamiltonian 1-norm, we set a tighter bound on τ to be $\tau \leq \frac{\pi\hbar}{2\|\hat{H}\|_1}$. Accordingly, we fixed $\tau = \frac{\pi\hbar}{10\|\hat{H}\|_1}$ and set $M = 10$. We then tested three Trotterization error thresholds corresponding to 9, 19, and 42 steps, as illustrated in Fig. 3. For all three configurations, we evaluated the autocorrelation function $C(t) = |\langle \psi_0 | \psi(t) \rangle|^2$ with $R = 5, 10, 15$, where the reference states were chosen as the bitstrings with the largest measurement probabilities from the state $e^{-i(M-1)\tau\hat{H}} |\psi_0\rangle$, following the procedure in [41]. The accuracy of the results was validated against time evolution approximations obtained using QuTiP [50].

D. Microwave Absorption Spectra Computation via sQKFF

Most spin-defect-based platforms exhibit optical activity when interacting with microwave magnetic fields. This property forms the foundation of the Optical Detection of Magnetic Resonance (ODMR) technique, which has been crucial in achieving precise measurements and

high-fidelity control over the spin quantum state. Spin defects are promising candidates for quantum technologies due to the capacity to manipulate the spin state reliably, e.g., via coupling to the magnetic component of incident electromagnetic waves, combined with coherence times long enough to apply these interactions effectively [51].

Research focusing on the applications and operational enhancement of spin defects through microwave and optical frequency interactions is highly active. The resulting applications span a wide range of quantum technologies, including quantum memories, scalable quantum computing and sensing, as well as enabling connections to photonic architectures for the implementation of quantum networks [52–55]. Therefore, providing a way to calculate the microwave absorption spectra would demonstrate the operational utility of simulating these spin-defect-based platforms, advancing the study and development of these systems for quantum technologies.

Linear response applies when the perturbation is sufficiently weak, and the system is initially in a stationary state of \hat{H}_0 (typically thermal equilibrium). We assume a static bias field defining the \hat{z} quantization axis and probe the system with a weak transverse oscillating magnetic field,

$$\hat{H}_P(t) = -B_x \cos(\omega t) \hat{M}_x. \quad (8)$$

In the long-wavelength limit $\lambda \gg L$, where L is the length scale of the system of interest, the driving field is effectively uniform across the spin ensemble; this is the magnetic dipole approximation, which we adopt in the forthcoming. For NV⁻ center configurations, \hat{M}_x is the x -component of the total magnetic moment, including the electronic spin operator \hat{S}_x and nuclear spin operators $\hat{I}_x^{(j)}$, with each contribution weighted by its gyromagnetic ratio.

The linear absorption spectrum is derived from the imaginary part of the generalized susceptibility $\chi(\omega)$, which corresponds to the Fourier transform of the re-

tarded commutator function,

$$C(t) = -i \left\langle \psi_0 \left| [e^{it\hat{H}} \hat{M}_x e^{-it\hat{H}}, \hat{M}_x] \right| \psi_0 \right\rangle \quad (9)$$

where \hat{H} is the stationary system's Hamiltonian. The power absorbed per unit of time is proportional to $\omega\chi''(\omega)$, where $\chi''(\omega)$ denotes the imaginary part of the susceptibility. The function $C(t)$ is related with the imaginary part of a function $Z(t)$, defined as

$$\begin{aligned} Z(t) &= \left\langle \psi_0 \left| e^{it\hat{H}} \hat{M}_x e^{-it\hat{H}} \hat{M}_x \right| \psi_0 \right\rangle \\ &= \left\langle \psi(t) \left| \hat{M}_x \right| \eta(t) \right\rangle, \end{aligned} \quad (10)$$

with $|\eta(t)\rangle = e^{-it\hat{H}} \hat{M}_x |\psi_0\rangle$. The sQKFF algorithm is employed to compute $Z(t)$ by approximating the time evolution of the states within the Krylov subspace $|\psi(t)\rangle = \sum_{m,r} c_m^\psi(t) |\phi_{mr}^\psi\rangle$ and $|\eta(t)\rangle = \sum_{m',r'} c_{m'r'}^\eta(t) |\phi_{m'r'}^\eta\rangle$. Note that the sets of reference bitstrings used for each state differ. This leads to the approximation

$$Z(t) \approx (\mathbf{c}^\psi(t))^\dagger A \mathbf{c}(t)^\eta, \quad (11)$$

where the $\mathbf{c}(t)$ vectors are obtained by solving Eq. 6 for the states $|\psi_0\rangle$ and $|\eta_0\rangle = \hat{M}_x |\psi_0\rangle$, and A is an $MR \times MR'$ matrix with elements $A_{(mr),(m'r')} = \left\langle \phi_{mr}^\psi \left| \hat{M}_x \right| \phi_{m'r'}^\eta \right\rangle$. These matrix elements, which implement the non-unitary operator \hat{M}_x , are computed using Hadamard tests combined with an LCU decomposition of \hat{M}_x .

E. ℓ_1 -norm of coherence with sQKFF

Assessing the coherence time of a quantum system typically requires comparing the coherence of its time-evolved state against that of the initial state. A plethora of coherence measures have been proposed in the literature to quantify this basis-dependent resource [56–65]. Among these, one of the widely employed resource quantifiers is the ℓ_1 -norm of coherence [58] due to its operational clarity.

Expressing the state of an n -qubit quantum system, $\hat{\rho}$, in the computational basis $\Theta \equiv \{|i\rangle \mid i \in \{0,1\}^n\}$, the ℓ_1 -norm of coherence, denoted $C_{\ell_1}(\hat{\rho})$, is given by

$$C_{\ell_1}(\hat{\rho}) = \sum_{\{i \neq j \mid i,j \in \Theta\}} |\langle i | \hat{\rho} | j \rangle|. \quad (12)$$

From the above definition, it is evident that measuring coherence is experimentally costly. For a density matrix representing the state of the system, computing $2^{2n} - 2^n$ off-diagonal parameters is required in the worst-case scenario. Moreover, when studying dynamics, the cost escalates further, as coherence must be evaluated at every time point. However, when the system evolves within a Krylov subspace, this overhead can be significantly reduced.

The system studied in this work is a number \mathcal{N} of NV[−] centers coupled with an environment, which includes the nuclear spins of each NV[−] center, the spin of ¹⁴N impurities, and a phonon bath. Considering it as a bipartite system composed of subsystems A , the NV[−] electronic spins, and B , their environment, the time-evolved state of the complete system is

$$|\psi\rangle_{AB} \equiv |\psi(t)\rangle = e^{-it\hat{H}/\hbar} |\psi_0\rangle, \quad (13)$$

which is approximated by Eq. 5. Then, in the Krylov approximation, the ℓ_1 -norm as defined in Eq. 12 can be expressed as

$$C_{\ell_1}(|\psi\rangle\langle\psi|_{AB}) = \sum_{\{k \neq l \mid k,l \in \Sigma \times \Gamma\}} \left| \sum_{m,r} \sum_{m',r'} c_{mr}(t) c_{m'r'}^*(t) \langle k | \phi_{mr} \rangle \langle \phi_{m'r'} | l \rangle \right|, \quad (14)$$

with binary alphabets Σ and Γ for subsystems A and B , respectively, such that their computational basis are $\{|a\rangle \mid a \in \Sigma\}$ and $\{|b\rangle \mid b \in \Gamma\}$.

Now, computing the coherence of the state at any time is only dependent on classically obtaining $\mathbf{c}(t)$ from Eq. 6, which doesn't require an additional quantum effort provided we already solved the Krylov subspace problem. The amplitudes of the corresponding computational basis states that compose the reference states $|\phi_{mr}\rangle$ can always be obtained via Hadamard tests, and remain the

same at all times t . However, since it is usual for reference states to be classically tractable, and we require only inner products of these states with computational basis bitstrings, the extra computational efforts required to compute the ℓ_1 norm are typically classical. Thus, while the process of computing the amplitudes may scale exponentially with the number of qubits, all subsequent coherence evaluations are efficient.

Tracing out the environment and rearranging terms yields a simplified expression for computing the ℓ_1 norm

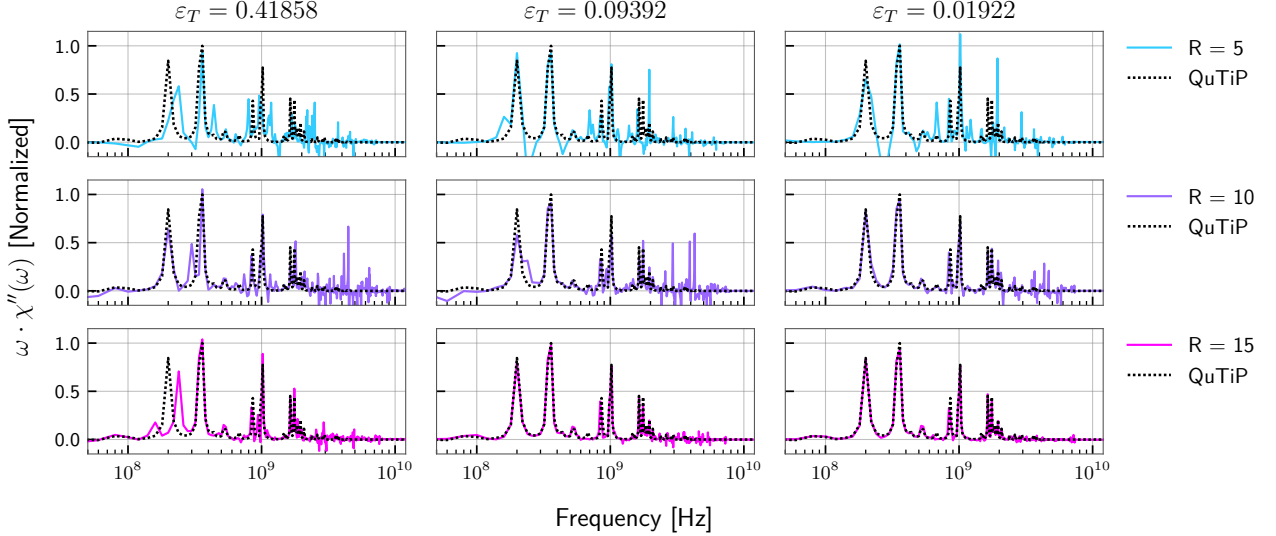


FIG. 4. Microwave absorption spectra comparison for Configuration 1. The plot shows the spectrum computed using QuTiP versus spectra calculated using sQKFF, for different numbers of reference states and Trotterization error thresholds. All spectra are normalized by the maximum intensity value of the spectrum computed using QuTiP.

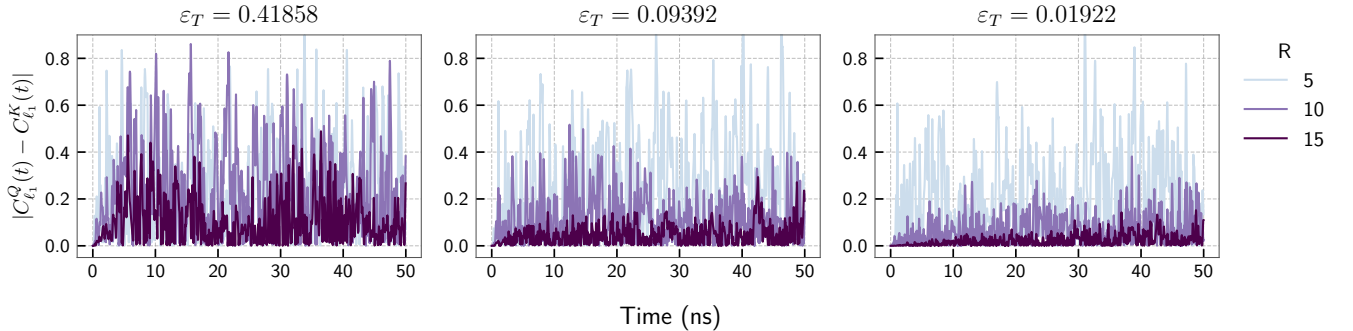


FIG. 5. Time evolution of the absolute value of the difference between the ℓ_1 -norm of coherence computed with QuTiP, $C_{\ell_1}^Q$, and those computed using the sQKFF algorithm, $C_{\ell_1}^Q$, for Configuration 1 and for different values of Trotterization thresholds and numbers of reference states, R .

of coherence of our system of interest: the NV[−] electronic spins, given by

$$C_{\ell_1}(\hat{\rho}_A) = \sum_{\{i \neq j \mid i, j \in \Sigma\}} \sum_{\{b \mid b \in \Gamma\}} |\gamma_{ib}\gamma_{jb}^*| \quad (15)$$

with $\gamma_{ib} = \sum_{mr} c_{mr}(t) \langle ib | \phi_{mr} \rangle$, where $|ib\rangle = |i\rangle \otimes |b\rangle$. Hence, the coherence of the subsystem's evolved state can be computed efficiently once the reference states' amplitudes are known. As a direct consequence, within the Krylov subspace, it is efficient to determine the time t when the coherence of the system decays to $1/e$ of its initial value, thus providing valuable information related to effective T_1 and T_2 coherence times.

III. RESULTS,

The comparison of the microwave absorption spectra of Configuration 1 is presented in Fig. 4, and it demonstrates that even with low-accuracy Trotterization thresholds, the spectra computed within our framework provide reliable initial insights into the expected resonance frequencies of the NV[−] system under external perturbation, such as incident microwave photons. As anticipated, the agreement with the spectrum calculated using QuTiP is improved by reducing the Trotterization error and increasing the number of reference states, successfully resolving all significant spectral peaks. Given that the absorption spectrum characterizes the dynamic response of the system to external fields, the high accuracy achieved confirms the utility of our framework for accurately calculating operational properties of these

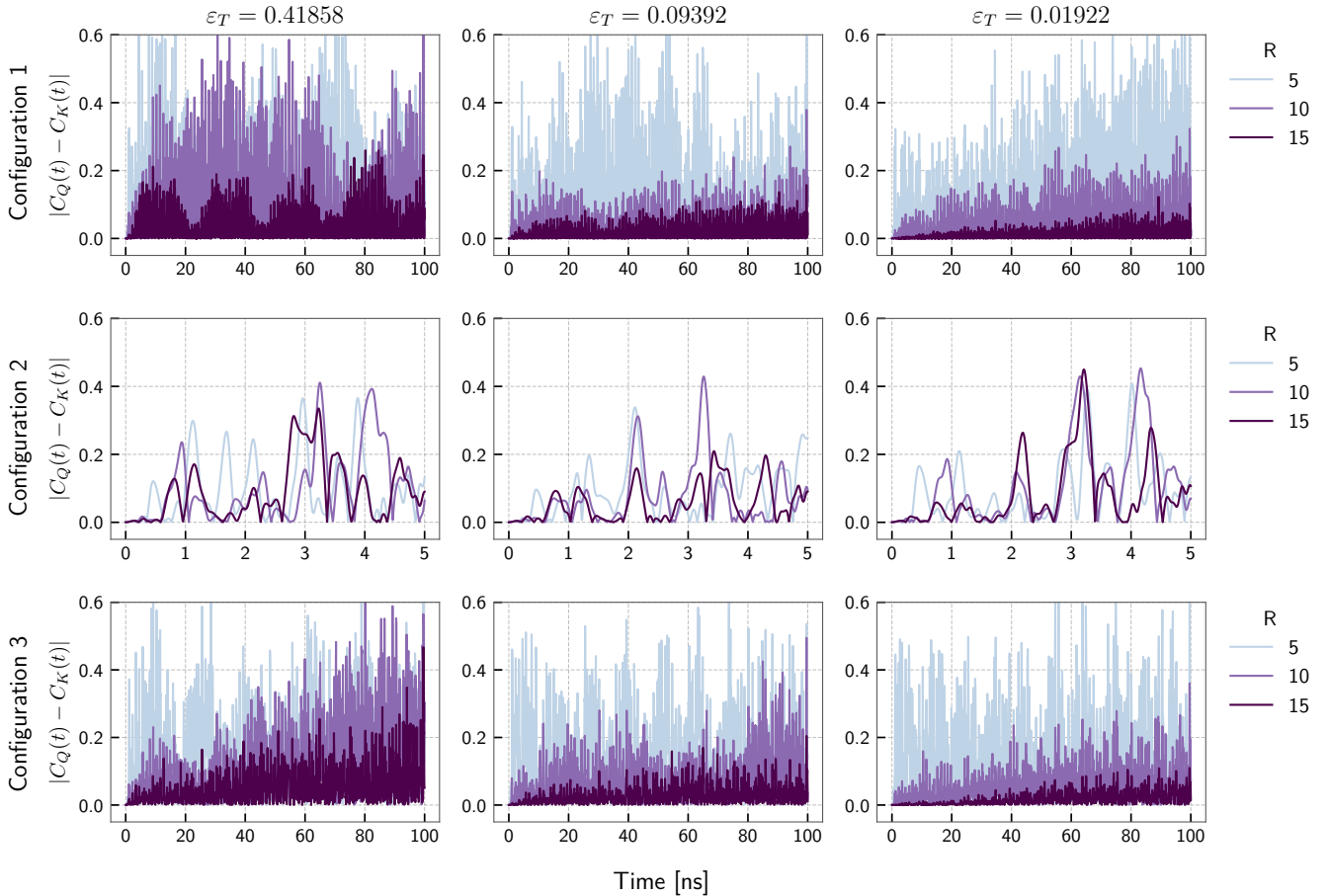


FIG. 6. Time evolution of the absolute value of the difference between the autocorrelation functions computed with QuTiP, $C_Q(t)$, and those obtained using sQKFF, $C_K(t)$, for all configurations and for different numbers of reference states, R .

spin defect-based platforms, which supports their study, modeling, and advancement.

In addition, the results for the computation of the ℓ_1 -norm of coherence for Configuration 1, shown in Fig. 5, exhibit a dependence on both the Trotterization error ε_T and the number of reference states R that is consistent with the behavior observed for the microwave absorption spectra, Fig. 4. While reducing ε_T predictably improves accuracy, increasing the number of reference states emerges as an effective way to achieve accurate results at operationally relevant timescales while maintaining feasible quantum resource requirements. This observation motivates further investigation into improved methods for reference-state selection.

The results presented in Fig. 6 illustrate the influence of ε_T and R on the performance of the sQKFF algorithm when computing the autocorrelation functions. For Configurations 1 and 3, these reproduce QuTiP results with good accuracy up to several tens of nanoseconds. A remarkable observation from these configurations is that the autocorrelation function can be simulated with reasonable precision for short times, approximately up to 20

nanoseconds, even when larger Trotterization errors are used. This implies that shorter quantum circuits with fewer gates can still yield meaningful results, thereby expediting computation. Nonetheless, increasing the number of reference states has a more pronounced effect, improving both the accuracy of the simulation and the achievable time span.

In particular, the results for Configuration 3 with $\varepsilon_T = 0.01922$ and $R = 15$ are noteworthy. Despite involving a more complex system with additional impurities, a larger number of qubits, and dipole–dipole interactions with the NV[−] center, its autocorrelation function exhibits a close agreement with the QuTiP results, comparable with that of Configuration 1, which represents a smaller system. These findings suggest that the selection of reference states plays a more decisive role in achieving accurate long-time dynamics than either the Trotterization error, which in our framework relates to the τ parameter, or system size. Consequently, a more informed or adaptive selection of reference states, chosen to better capture the relevant features of the long-time evolution, could enable accurate simulations while sub-

ε_T	0.41858			0.09392			0.01922		
Metric	\mathcal{W}	\mathcal{G}	γ	\mathcal{W}	\mathcal{G}	γ	\mathcal{W}	\mathcal{G}	γ
Configuration 1									
Hadamard	1.6	1.2	0.2717	3.4	2.5	0.2720	7.5	5.5	0.2722
CNOT	4.4	3.1	0.2994	9.3	6.5	0.2994	20.5	14.4	0.2995
T	82.3	64.3	0.2187	173.6	135.6	0.2189	383.7	299.6	0.2190
Circuit Depth	7.5	5.3	0.2916	15.9	11.3	0.2917	35.1	24.9	0.2917
Configuration 2									
Hadamard	6.4	4.7	0.2684	13.5	9.9	0.2685	29.8	21.8	0.2685
CNOT	18.5	13.4	0.2780	39.1	28.2	0.2780	86.5	62.4	0.2781
T	320.6	250.2	0.2196	676.6	528.0	0.2197	1495.4	1166.9	0.2197
Circuit Depth	31.4	22.8	0.2734	66.3	48.2	0.2734	146.5	106.5	0.2735
Configuration 3									
Hadamard	3.1	2.3	0.2362	6.5	4.9	0.2363	14.3	10.9	0.2364
CNOT	8.5	6.3	0.2565	17.9	13.3	0.2565	39.5	29.4	0.2565
T	156.5	126.9	0.1895	330.3	267.7	0.1896	730.0	591.6	0.1897
Circuit Depth	14.4	10.8	0.2504	30.5	22.9	0.2504	67.4	50.5	0.2505

TABLE II. Resource estimations for the Hadamard test circuit in all configurations, evaluated under different ε_T . The column $\mathcal{W} [\times 10^4]$ reports the metric values without QWC aggregation, while $\mathcal{G} [\times 10^4]$ shows the corresponding values when aggregation is applied. The ratio γ quantifies the relative reduction between \mathcal{W} and \mathcal{G} . The number of T gates per Rz rotation was estimated with precision $\varepsilon = 10^{-6}$ [66].

stantially reducing the computational overhead on quantum hardware.

The importance of reference state selection is supported by the results for Configuration 2 shown in Fig. 6. Owing to the larger system size, the set of measured bitstrings from the state $e^{-i(M-1)\tau\hat{H}}|\psi(t=0)\rangle$ with the highest probabilities, from which the reference states are selected, contains a substantially greater number of elements. As a result, information about the system dynamics becomes more sparsely distributed across the possible states, making it more difficult to identify reference states that effectively capture the features relevant to long-time dynamics.

Another factor distinguishing Configuration 2 from Configurations 1 and 3 is the value of the Hamiltonian 1-norm. For Configuration 2, we obtained $\|\hat{H}\|_1/\hbar = 112.265$ GHz, whereas Configurations 1 and 3 yielded 62.1052 and 62.1124 GHz, respectively. In our framework, the Hamiltonian's 1-norm directly influences the sQKFF algorithm through the dependence of τ on $\|\hat{H}\|_1$, which in turn affects the construction of the reference states. This observation naturally leads to the following question: *Is there a specific time $T = (M-1)\tau$ at which the measured bitstrings, subsequently used as reference states, encode more meaningful information about the system's long-time dynamics?* Addressing this question would require systematic studies to determine whether such a characteristic time exists and how it may depend on the interplay between the system's Hamiltonian norm, the number of reference states, and the Trotterization error. Further investigations towards a better method for reference state selection could provide valuable in-

sight into optimizing the sQKFF algorithm for enhanced stability and efficiency in simulating long-time quantum dynamics.

Finally, resource estimations for the quantum circuits used to compute the elements of the S and H matrices are summarized in Tab. II. These indicate that a substantial reduction in computational resources is achieved through QWC aggregation. Moreover, the reduction ratio γ remains nearly constant as the Trotter error threshold ε_T increases. Since each step of the Trotterized time-evolution operator involves the repeated application of the same operator, the resource reduction per step is expected to be consistent with that of the overall circuit, with minor variations arising only from cancellations of adjacent operations between steps.

IV. ADDITIONAL CONSIDERATIONS AND OUTLOOK

The framework presented in this work shows that simulating the dynamics of the quantum system over short timescales can enable access to physically and operationally relevant regimes. In particular, our numerical results using a few picoseconds of quantum simulation show excellent agreement with exact simulations up to 50-100 nanoseconds. This proof of principle indicates that, even under restrained resources and hardware noise, quantum computers combined with optimized simulation techniques can serve as effective platforms for studying the properties and dynamics of spin-defects in solid-state materials. Advancing toward practical implementation

on real quantum hardware will require addressing additional considerations, such as the number of measurement shots, crucial for accurately estimating expectation values [67, 68], as well as the number of qubits and their limited connectivity [69, 70]. The former is relevant because the sQKFF algorithm relies on computing the expectation value of the Hamiltonian, whereas the latter becomes particularly relevant when simulating quantum systems with non-trivial interactions, such as the dipole-dipole coupling present in Configurations 2 and 3, which introduces a large number of entangled pairs.

Further analysis of measurement cost will be essential to assess the feasibility of sQKFF on real quantum hardware. Krylov-subspace approaches are notoriously sensitive to noise because the overlap matrix S is often ill-conditioned, so practical implementations typically regularize by projecting onto the subspace associated with eigenvalues above a chosen threshold [71, 72]. In sQKFF, finite-shot Hadamard tests introduce statistical fluctuations in the estimated elements of S and H , as well as in the probability distributions used for reference-state selection, and these fluctuations can be amplified by the conditioning of S . Consequently, although each circuit instance can be shallow, achieving additive precision ϵ in the required matrix elements by direct sampling generally demands $\mathcal{O}(1/\epsilon^2)$ repetitions, so wall-clock time can be dominated by shot count when executions are serialized. Two complementary mitigations are available: using recent advances to reduce shot overhead [73], including new subspace methods that exploit symmetries to reduce the number of distinct Hamiltonian terms that must be measured, resulting in substantial shot savings [74], and circuit repetitions can be parallelized between multiple QPUs using distributed execution strategies by shot [75, 76]. Alternatively, when coherent access to the circuit (and its inverse) is available, one can replace classical sampling with amplitude-estimation variants of the Hadamard test, which reduce the query complexity to $\mathcal{O}(1/\epsilon)$ at the cost of deeper, controlled circuits [77]. Beyond measurement overhead, our results indicate that long-time accuracy is primarily limited by reference-state choice: selecting states to maximize overlap with either the initial state or a short-time evolved state is insufficient, motivating more dynamics-aware selection criteria that can achieve reliable long-time evolution with fewer Trotter steps and reduced quantum resources.

V. SUMMARY AND CONCLUSIONS

In this work, a framework for simulating and characterizing spin-defects in solid-state materials is proposed, aiming to support the research of current and new platforms for quantum technologies. The framework integrates multiple resource-optimization strategies within the PennyLane library, including Hamiltonian mapping via Gray encoding, qubit-wise commuting aggregation, and the multi-reference, selected Quantum Krylov Fast-

Forwarding algorithm. Three NV⁻ configurations were analyzed, incorporating interactions found in experimental setups. This hybrid approach enabled the evaluation of autocorrelation functions, absorption spectra, and ℓ_1 -norm of coherence at extended timescales, while providing detailed estimations of quantum resources under different Trotterization thresholds and numbers of reference states.

High-precision autocorrelation functions were achieved for Configurations 1 and 3; microwave absorption spectra and ℓ_1 -norm of coherence were also computed for Configuration 1. All these results reproduced QuTiP simulations over tens of nanoseconds, even under moderate Trotterization errors. Increasing the number of reference states had the greatest impact on both accuracy and simulated time range, while qubit-wise commuting aggregation consistently reduced quantum resource requirements by 18–30% across all configurations. These results highlight the potential of the multi-reference, selected Quantum Krylov Fast-Forwarding algorithm as a scalable tool for simulating complex quantum dynamics on NISQ and early fault-tolerant devices.

While quantum technologies provide promising and theoretically advantageous approaches to addressing real-world problems, the current hardware available in the NISQ and early fault-tolerant eras remains constrained by limited resources. Our work demonstrates how integrating different techniques can harness the natural suitability of digital quantum computers for simulating quantum systems, enabling reduced resource requirements and extended operational timescales in the design and characterization of next-generation quantum technologies based on spin defects in solid-state materials.

The ability to simulate complex dynamics across configurations that are classically intractable may prove crucial for advancing quantum device engineering and overcoming present technological limitations. Nevertheless, this study also highlights the inherent challenges of simulating quantum systems with non-trivial interactions, both operationally and methodologically. Although the digital simulation of the time evolution of such systems remains a long-term objective, it is a feasible and worthwhile pursuit that holds substantial promise for the continued development of quantum technologies.

KEY SOFTWARE PACKAGES

The framework was implemented using PennyLane v0.42 and Catalyst v0.12 [78], with numerical results compared against approximated solutions obtained with QuTiP v5.2.1 [50]. QuTiP solutions were computed using the `sesolve` function with `adams` method for ODE integration, absolute tolerance 10^{-5} , and relative tolerance 10^{-6} .

ACKNOWLEDGMENTS

The authors acknowledge the Quantum Open Source Foundation Mentorship Program for enabling the participation of students interested in quantum technologies in research projects such as the one presented here.

We extend our thanks to Kevin Ferreira, Yipeng Ji and Paria Nejat of the LG Electronics Toronto AI Lab and to Sean Kim of LG Electronics, AI Lab, for their ongoing support of our research.

-
- [1] M. Maciaszek and B. Baur, Cbvb-nh complexes as prevalent defects in metal-organic vapor-phase epitaxy-grown hexagonal boron nitride (2025), [arXiv:2510.14012 \[cond-mat.mtrl-sci\]](#).
- [2] T. Vogl, V. Ivády, I. J. Luxmoore, and H. L. Stern, Defects in hexagonal boron nitride for quantum technologies (2025), [arXiv:2510.04344 \[cond-mat.mes-hall\]](#).
- [3] O. Rubinas, M. Petrov, E. Bourgeois, J. Hruba, M. Nesladek, *et al.*, Electrical readout of spin environments in diamond for quantum sensing (2025), [arXiv:2509.26570 \[quant-ph\]](#).
- [4] S. G. Carter, I. Tathfif, C. Burgess, B. VanMil, S. Debata, and P. Dev, The influence of nitrogen doping and annealing on the silicon vacancy in 4h-sic (2025), [arXiv:2506.17478 \[cond-mat.other\]](#).
- [5] J. F. Barry, J. M. Schloss, E. Bauch, M. J. Turner, R. L. Walsworth, *et al.*, Sensitivity optimization for NV-diamond magnetometry, *Rev. Mod. Phys.* **92**, 10.1103/RevModPhys.92.015004 (2020), [arXiv:1903.08176](#).
- [6] B. Rodiek, M. Lopez, H. Hofer, G. Porrovecchio, M. Smid, S. Kuck, *et al.*, Experimental realization of an absolute single-photon source based on a single nitrogen vacancy center in a nanodiamond, *Optica* **4**, 71 (2017).
- [7] H. Park, J. Lee, S. Han, S. Oh, and H. Seo, Decoherence of nitrogen-vacancy spin ensembles in a nitrogen electron-nuclear spin bath in diamond, *npj Quantum Inf.* **8**, 1 (2022).
- [8] D. Suter and F. Jelezko, Single-spin magnetic resonance in the nitrogen-vacancy center of diamond, *Prog. Nucl. Magn. Reson. Spectrosc.* **98-99**, 50 (2017).
- [9] T. H. Kyaw, T. Menke, S. Sim, A. Anand, N. P. D. Sawaya, A. Aspuru-Guzik, *et al.*, Quantum Computer-Aided Design: Digital Quantum Simulation of Quantum Processors, *Phys. Rev. Appl.* **16**, 044042 (2021).
- [10] J. S. Kottmann, M. Krenn, T. H. Kyaw, S. Alperin-Lea, and A. Aspuru-Guzik, Quantum computer-aided design of quantum optics hardware, *Quantum Sci. Technol.* **6**, 035010 (2021).
- [11] I. Georgescu, S. Ashhab, and F. Nori, Quantum simulation, *Rev. Mod. Phys.* **86**, 153–185 (2014).
- [12] W. Li, Z. Yin, X. Li, D. Ma, S. Yi, S. Zhang, *et al.*, A hybrid quantum computing pipeline for real world drug discovery, *Sci. Rep.* **14**, 10.1038/s41598-024-67897-8 (2024).
- [13] R. Santagati, A. Aspuru-Guzik, R. Babbush, M. Degroote, L. González, C. Utschig-Utschig, *et al.*, Drug design on quantum computers, *Nat. Phys.* **20**, 549–557 (2024).
- [14] M. V. Jabir, N. F. R. Annafianto, I. A. Burenkov, A. Battou, and S. V. Polyakov, Energy and bandwidth efficiency optimization of quantum-enabled optical communication channels, *npj Quantum Inf.* **8**, 10.1038/s41534-022-00573-9 (2022).
- [15] Q. Wu, D. Ribezzo, G. Di Sciullo, S. Cocchi, D. Ann Shaji, C. Antonelli, *et al.*, Integration of quantum key distribution and high-throughput classical communications in field-deployed multi-core fibers, *Light Sci. Appl.* **14**, 10.1038/s41377-025-01982-z (2025).
- [16] Y. Shao, Y. Gong, X. Wan, X. Huang, T. Zhang, *et al.*, Quantum-enabled topological optimization of distributed energy storage for resilient black-start operations, *Sci. Rep.* **15**, 10.1038/s41598-025-02286-3 (2025).
- [17] W. Hou, W. Yao, X. Zhao, K. Rehan, J. Du, *et al.*, Combining energy efficiency and quantum advantage in cyclic machines, *Nat. Commun.* **16**, 10.1038/s41467-025-60179-5 (2025).
- [18] Z. Yin, I. Agresti, G. de Felice, D. Brown, A. Toumi, P. Walther, *et al.*, Experimental quantum-enhanced kernel-based machine learning on a photonic processor, *Nat. Photon.* **19**, 1020–1027 (2025).
- [19] G. Pallavi, A. Altalbe, and R. P. Kumar, Qkdti a quantum kernel based machine learning model for drug target interaction prediction, *Sci. Rep.* **15**, 10.1038/s41598-025-07303-z (2025).
- [20] A. Kumar, S. Dhanka, A. Sharma, R. Bansal, M. Aljuaid, *et al.*, A hybrid framework for heart disease prediction using classical and quantum-inspired machine learning techniques, *Sci. Rep.* **15**, 10.1038/s41598-025-09957-1 (2025).
- [21] C. Foreman, S. Wright, A. Edgington, M. Berta, and F. J. Curchod, Practical randomness amplification and privatisation with implementations on quantum computers, *Quantum* **7**, 969 (2023).
- [22] T. Qasim, V. A. Siris, I. Oosthuizen, M. Rajarajan, and S. Biswas, Quantum secure biometric authentication in decentralised systems (2026), [arXiv:2601.04852 \[cs.CR\]](#).
- [23] J. Preskill, Quantum computing in the NISQ era and beyond, *Quantum* **2**, 1 (2018), [arXiv:1801.00862](#).
- [24] A. Katabarwa, K. Gratsea, A. Caesura, and P. D. Johnson, Early fault-tolerant quantum computing, *PRX Quantum* **5**, 10.1103/prxquantum.5.020101 (2024).
- [25] A. M. Childs, D. Maslov, Y. Nam, N. J. Ross, and Y. Su, Toward the first quantum simulation with quantum speedup, *Proc. Natl. Acad. Sci. U.S.A.* **115**, 9456 (2018), [arXiv:1711.10980](#).
- [26] K. L. Brown, W. J. Munro, and V. M. Kendon, Using Quantum Computers for Quantum Simulation, *Entropy* **12**, 2268 (2010), [arXiv:1004.5528](#).
- [27] Google Quantum AI and Collaborators, Observation of constructive interference at the edge of quantum ergodicity, *Nature* **646**, 825 (2025).
- [28] C. Zhang, R. G. Cortiñas, A. H. Karamlou, N. Noll, J. Provazza, T. E. O'Brien, *et al.*, Quantum computation of molecular geometry via many-body nuclear spin echoes (2025), [arXiv:2510.19550 \[quant-ph\]](#).

- [29] T. E. O'Brien, W. D. Oliver, A. Opremcak, *et al.*, Quantum computation of molecular structure using data from challenging-to-classically-simulate nuclear magnetic resonance experiments, *PRX Quantum* **3**, 030345 (2022).
- [30] B. Huang, M. Govoni, and G. Galli, Simulating the electronic structure of spin defects on quantum computers, *PRX Quantum* **3**, 010339 (2022).
- [31] J. S. Baker, P. A. M. Casares, M. Shokrian Zini, J. Thik, D. Banerjee, J. M. Arrazola, *et al.*, Simulating optically-active spin defects with a quantum computer, *Phys. Rev. A* **110**, 032606 (2024).
- [32] P. A. M. Casares, Y. Zhou, U. Azad, S. Fomichev, J. S. Baker, J. M. Arrazola, *et al.*, Quantum algorithms to detect odmr-active defects for quantum sensing applications (2025), [arXiv:2508.13281 \[quant-ph\]](https://arxiv.org/abs/2508.13281).
- [33] N. Sheng, C. Vorwerk, M. Govoni, and G. Galli, Green's function formulation of quantum defect embedding theory, *J. Chem. Theory Comput.* **18**, 3512–3522 (2022).
- [34] S. Chen, V. W.-z. Yu, Y. Jin, M. Govoni, and G. Galli, Advances in quantum defect embedding theory, *J. Chem. Theory Comput.* **21**, 7797–7812 (2025).
- [35] A. M. Childs, Y. Su, M. C. Tran, N. Wiebe, and S. Zhu, Theory of trotter error with commutator scaling, *Physical Review X* **11**, 10.1103/physrevx.11.011020 (2021).
- [36] S. Gu, R. D. Somma, and B. Şahinoğlu, Fast-forwarding quantum evolution, *Quantum* **5**, 577 (2021).
- [37] C. Cîrstoiu, Z. Holmes, J. Iosue, L. Cincio, P. J. Coles, and A. Sornborger, Variational fast forwarding for quantum simulation beyond the coherence time, *npj Quantum Inf.* **6**, 10.1038/s41534-020-00302-0 (2020).
- [38] B. Commeau, M. Cerezo, Z. Holmes, L. Cincio, P. J. Coles, and A. Sornborger, Variational hamiltonian diagonalization for dynamical quantum simulation (2020), [arXiv:2009.02559 \[quant-ph\]](https://arxiv.org/abs/2009.02559).
- [39] Z.-X. Shang, N. Guo, P. Rebentrost, A. Aspuru-Guzik, T. Li, and Q. Zhao, Fast-forwardable lindbladians imply quantum phase estimation (2025), [arXiv:2510.06759 \[quant-ph\]](https://arxiv.org/abs/2510.06759).
- [40] T. Ko, S. Choi, H. Park, and X. Li, Classical optimization algorithms for diagonalizing quantum hamiltonians (2025), [arXiv:2506.17883 \[quant-ph\]](https://arxiv.org/abs/2506.17883).
- [41] C. L. Cortes, A. E. DePrince, and S. K. Gray, Fast-forwarding quantum simulation with real-time quantum krylov subspace algorithms, *Phys. Rev. A* **106**, 10.1103/physreva.106.042409 (2022).
- [42] V. Verteletskyi, T.-C. Yen, and A. F. Izmaylov, Measurement optimization in the variational quantum eigen-solver using a minimum clique cover, *J. Chem. Phys.* **152**, 10.1063/1.5141458 (2020).
- [43] J. Izaac, Measurement optimization, https://pennylane.ai/qml/demos/tutorial_measurement_optimize (2021), date Accessed: 2026-01-27.
- [44] C. Kokail, P. E. Dolgirev, R. van Bijnen, D. Gonzalez-Cuadra, M. D. Lukin, and P. Zoller, Inverse quantum simulation for quantum material design (2026), [arXiv:2601.12239 \[quant-ph\]](https://arxiv.org/abs/2601.12239).
- [45] G. X. Wang, Y. K. Wu, R. Yao, W. Q. Lian, Z. J. Cheng, L. M. Duan, *et al.*, Simulating the spin-boson model with a controllable reservoir in an ion trap (2024), [arXiv:2402.07461 \[quant-ph\]](https://arxiv.org/abs/2402.07461).
- [46] S. Felton, A. M. Edmonds, M. E. Newton, P. M. Martineau, D. Fisher, and D. J. Twitchen, Electron paramagnetic resonance studies of the neutral nitrogen vacancy in diamond, *Phys. Rev. B* **77**, 10.1103/physrevb.77.081201 (2008).
- [47] M. Steiner, P. Neumann, J. Beck, F. Jelezko, and J. Wrachtrup, Universal enhancement of the optical readout fidelity of single electron spins at nitrogen-vacancy centers in diamond, *Phys. Rev. B* **81**, 10.1103/physrevb.81.035205 (2010).
- [48] N. P. D. Sawaya, T. Menke, T. H. Kyaw, S. Johri, A. Aspuru-Guzik, and G. G. Guerreschi, Resource-efficient digital quantum simulation of d-level systems for photonic, vibrational, and spin-s hamiltonians, *npj Quantum Inf.* **6**, 10.1038/s41534-020-0278-0 (2020).
- [49] C. L. Cortes and S. K. Gray, Quantum krylov subspace algorithms for ground- and excited-state energy estimation, *Phys. Rev. A* **105**, 10.1103/physreva.105.022417 (2022).
- [50] N. Lambert, E. Giguère, P. Menczel, B. Li, P. Hopf, F. Nori, *et al.*, Qutip 5: The quantum toolbox in python (2025), [arXiv:2412.04705 \[quant-ph\]](https://arxiv.org/abs/2412.04705).
- [51] H.-H. Fang, X.-J. Wang, X. Marie, and H.-B. Sun, Quantum sensing with optically accessible spin defects in van der waals layered materials, *Light Sci. Appl.* **13**, 10.1038/s41377-024-01630-y (2024).
- [52] J. J. Morton and P. Bertet, Storing quantum information in spins and high-sensitivity esr, *J. Magn. Reson.* **287**, 128–139 (2018).
- [53] F. Cache, Y. Baron, B. Lefaucher, J.-B. Jager, F. Mazen, A. Dréau, *et al.*, A single optically detectable tumbling spin in silicon (2025), [arXiv:2510.15590 \[quant-ph\]](https://arxiv.org/abs/2510.15590).
- [54] J. Resch, I. Karapatzakis, M. Elshorbagy, M. Schrodin, P. Fuchs, D. Hunger, *et al.*, (2025), [arXiv:2509.03354 \[quant-ph\]](https://arxiv.org/abs/2509.03354).
- [55] M. F. F. Chowdhury, A. Jung, L. L. Spina, A. Bartasyte, S. Margueron, and J. Atulasimha, Energy efficient coherent quantum control of nitrogen vacancy (nv) spin with nanoscale magnets (2024), [arXiv:2407.14018](https://arxiv.org/abs/2407.14018).
- [56] A. Streltsov, G. Adesso, and M. B. Plenio, Colloquium: Quantum coherence as a resource, *Rev. Mod. Phys.* **89**, 041003 (2017).
- [57] J. Åberg, Quantifying superposition (2006), [arXiv:quant-ph/0612146 \[quant-ph\]](https://arxiv.org/abs/quant-ph/0612146).
- [58] T. Baumgratz, M. Cramer, and M. B. Plenio, Quantifying coherence, *Phys. Rev. Lett.* **113**, 140401 (2014).
- [59] X. Yuan, H. Zhou, Z. Cao, and X. Ma, Intrinsic randomness as a measure of quantum coherence, *Phys. Rev. A* **92**, 022124 (2015).
- [60] A. Albrecht, A. Retzker, F. Jelezko, and M. B. Plenio, Coupling of nitrogen vacancy centres in nanodiamonds by means of phonons, *New J. Phys.* **15**, 083014 (2013).
- [61] A. Winter and D. Yang, Operational resource theory of coherence, *Phys. Rev. Lett.* **116**, 120404 (2016).
- [62] E. Chitambar and G. Gour, Comparison of incoherent operations and measures of coherence, *Phys. Rev. A* **94**, 052336 (2016).
- [63] J. I. de Vicente and A. Streltsov, Genuine quantum coherence, *J. Phys. A: Math. Theory* **50**, 045301 (2016).
- [64] T. Theurer, D. Egloff, L. Zhang, and M. B. Plenio, Quantifying operations with an application to coherence, *Phys. Rev. Lett.* **122**, 190405 (2019).
- [65] G. Saxena, E. Chitambar, and G. Gour, Dynamical resource theory of quantum coherence, *Phys. Rev. Res.* **2**, 023298 (2020).
- [66] M. P. Harrigan, T. Khattar, C. Yuan, A. Peduri, N. C. Rubin, *et al.*, Expressing and analyzing quantum algorithms with qualtran (2024), [arXiv:2409.04643 \[quant-ph\]](https://arxiv.org/abs/2409.04643).

- ph].
- [67] O. Crawford, B. v. Straaten, D. Wang, T. Parks, E. Campbell, and S. Brierley, Efficient quantum measurement of pauli operators in the presence of finite sampling error, *Quantum* **5**, 385 (2021).
 - [68] T.-C. Yen and A. F. Izmaylov, Cartan subalgebra approach to efficient measurements of quantum observables, *PRX Quantum* **2**, 10.1103/prxquantum.2.040320 (2021).
 - [69] S. Brierley, Efficient implementation of quantum circuits with limited qubit interactions, *Quantum Inf. Comput.* **17**, 1096–1104 (2017).
 - [70] A. Holmes, S. Johri, G. G. Guerreschi, J. S. Clarke, and A. Y. Matsuura, Impact of qubit connectivity on quantum algorithm performance, *Quantum Sci. Technol.* **5**, 025009 (2020).
 - [71] W. Kirby, Analysis of quantum krylov algorithms with errors, *Quantum* **8**, 1457 (2024).
 - [72] N. Yoshioka, M. Amico, W. Kirby, P. Jurcevic, A. Dutt, A. Mezzacapo, *et al.*, Krylov diagonalization of large many-body hamiltonians on a quantum processor, *Nat. Commun.* **16**, 10.1038/s41467-025-59716-z (2025).
 - [73] G. Lee, S. Choi, J. Huh, and A. F. Izmaylov, Efficient strategies for reducing sampling error in quantum krylov subspace diagonalization, *Digital Discovery* **4**, 954–969 (2025).
 - [74] S. Patel, P. Jayakumar, R. Huang, T. Zeng, and A. F. Izmaylov, Quantum seniority-based subspace expansion: Linear combinations of short-circuit unitary transformations for the electronic structure problem (2025), arXiv:2509.01061 [quant-ph].
 - [75] G. Bisicchia, G. Clemente, J. Garcia-Alonso, J. M. Murillo, M. D’Elia, and A. Brogi, Distributing quantum computations, shot-wise, *Future Internet* **17**, 507 (2025).
 - [76] D. Barral, F. J. Cardama, G. Díaz-Camacho, D. Faúlde, I. F. Llovo, A. Gómez, *et al.*, Review of distributed quantum computing: From single qpu to high performance quantum computing, *Comput. Sci. Rev.* **57**, 100747 (2025).
 - [77] G. Brassard, P. Høyer, M. Mosca, and A. Tapp, Quantum amplitude amplification and estimation, in *Quantum Computation and Information*, Contemporary Mathematics, Vol. 305, edited by S. J. Lomonaco (American Mathematical Society, 2002) pp. 53–74, arXiv:quant-ph/0005055 [quant-ph].
 - [78] V. Bergholm, J. Izaac, M. Schuld, C. Gogolin, S. Ahmed, N. Killoran, *et al.*, PennyLane: Automatic differentiation of hybrid quantum-classical computations (2022), arXiv:1811.04968 [quant-ph].